

through them. Therein, the phase shifts of each SIM were optimised in an alternating optimisation (AO) manner based on instantaneous channel state information (CSI) conditions. In [16], we proposed a simultaneous optimization of the phase shifts of both the transmitter and the receiver. In [21], the authors deployed a SIM-enabled (base station) to perform downlink beamforming in the EM wave domain to multiple users. However, these works relied on perfect CSI to design the SIMs. In [22], a digital wave-based channel estimator was proposed, where multiple subphases were first precoded in the wave domain, and then, in the digital domain.

A. Contributions

The reflections above led us to the crux of this work, which is to introduce two SIMs in a mMIMO system with multiple users, one at the BS and one at the intermediate space under the assumptions of correlated fading and imperfect CSI, and study the uplink sum spectral efficiency (SE).

Our main contributions are summarised as follows:

- Under the general setup of a mMIMO BS, we propose a new architecture including two SIMs, and we obtain the uplink achievable SE with imperfect CSI and maximum-ratio combining (MRC) in closed form that hinges only on large-scale statistics based on the two time-scale protocol. Specifically, one SIM is integrated into the BS to enable decoding in the electromagnetic wave domain, and the other SIM is aimed to assist the communication between the users and the BS in the same domain.
- We perform channel estimation based on the linear minimum mean-squared error (LMMSE) method. We also remark that channel estimation of BSIM and CSIM-assisted mMIMO systems has not taken place before.
- Different from [21], not only do we consider a SIM-based BS, but we also consider a SIM in the intermediate space to aid the communication between the users and the BS. Also, we rely on statistical CSI instead of instantaneous-based analysis in [21]. Moreover, we consider imperfect CSI, which is of practical interest. Compared to [22], which considered several subfaces to estimate the channel in SIM-assisted multi-user systems, we manage to update the estimated channel in a single phase. Thus, the approach in [22], requiring too much overhead, reduces the SE, while our approach does not appear this significant disadvantage. Note that [22] assumes a simple SIM at the BS, while we consider an additional SIM at the intermediate space.
- The proposed optimization is based on statistical CSI, which means it can be executed at every several coherence intervals. As a result, we achieve reduced overhead and computational complexity. Previous works on SIM-based communications relied on instantaneous CSI, which changes at each coherence interval, and is not suitable for practical SIM-based systems that include many surfaces, and thus bring high burden.
- We conceive the problem optimizing the phase shifts of both SIMs. Despite the nonconvexity of this problem, we propose a projected gradient ancient method (PGAM),

which optimises the phase shifts of both SIMs simultaneously. This is a noteworthy contribution since [18] optimized the phase shifts in an AO way. We perform a comparison between the two approaches, and show the superiority of our approach.

- Simulations show the superiority of the proposed architecture, examine which SIM has the greatest impact, and shed light on the effect of various system parameters on the sum SE.

Paper Outline: The remainder of this paper is organized as follows. Section II describes the system and channel models of a BSIM and CSIM-assisted mMIMO system. Section III elaborates on the CE and the uplink data transmission with the obtained uplink sum SE. In Section IV, we present the problem formulation and the simultaneous optimization of both BSIM and CSIM. The numerical results are discussed in Section V. Section VI concludes the paper.

Notation: Vectors and matrices are described by boldface lower and upper case symbols, respectively. The notations $(\cdot)^T$, $(\cdot)^H$, and $\text{tr}(\cdot)$ denote the transpose, Hermitian transpose, and trace operators, respectively. The notation $\mathbb{E}[\cdot]$ expresses the expectation operator, and $\text{diag}(\mathbf{A})$ describes a vector with elements equal to the diagonal elements of \mathbf{A} . The notation $\text{diag}(\mathbf{x})$ denotes a diagonal matrix whose elements are \mathbf{x} , while $\mathbf{b} \sim \mathcal{CN}(\mathbf{0}, \mathbf{\Sigma})$ denotes a circularly symmetric complex Gaussian vector with zero mean and a covariance matrix $\mathbf{\Sigma}$. In the case of complex-valued \mathbf{x} and \mathbf{y} , we denote $\langle \mathbf{x}, \mathbf{y} \rangle = 2 \text{Re}\{\mathbf{x}^H \mathbf{y}\}$.

II. SYSTEM AND CHANNEL MODELS

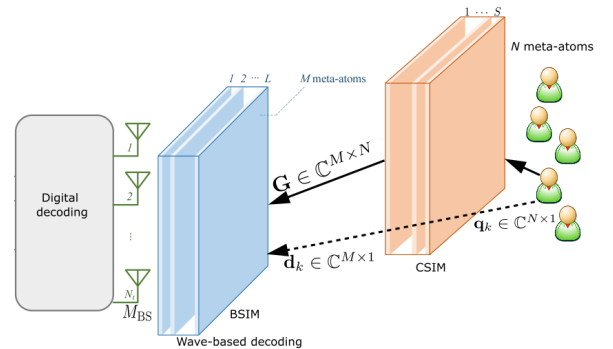


Fig. 1: A BSIM and CSIM-assisted mMIMO system with multiple users.

A. System Model

We consider the uplink of a multiuser MISO wireless system, where the BS is equipped with a large number of M_{BS} antennas that serve K single-antennas users under the same time-frequency resources. In this context, we employ the BSIM, integrated into the BS to enable receive decoding in the EM wave domain, and the CSIM to enhance the communication between the users and the BS in the wave domain, as shown in Fig. 1. For the fabrication of BSIM, we utilize an array of L metasurfaces, where each one of

them consists of M meta-atoms. The corresponding sets are $\mathcal{L} = \{1, \dots, L\}$ and $\mathcal{M} = \{1, \dots, M\}$. Similarly, the CSIM includes an array of S metasurfaces, each including N meta-atoms.¹ The corresponding sets are $\mathcal{S} = \{1, \dots, S\}$ and $\mathcal{N} = \{1, \dots, N\}$. Both SIMs are connected to independent smart controllers, which can adjust the corresponding phase shifts of the EM waves that are transmitted through each of their meta-atoms. Note that the forward propagation process in each SIM resembles a fully connected ANN, where training the interconnection architecture of the BSIM enables uplink decoding, while the respective training of the CSIM enables shaping the propagation environment. We denote $\Phi^l = \text{diag}(\phi^l) \in \mathbb{C}^{M \times M}$, where $\phi^l = [\phi_1^l, \dots, \phi_M^l]^T \in \mathbb{C}^{M \times 1}$ is the transmission coefficient matrix of the BSIM. Note that $\phi_m^l = e^{j\theta_m^l}$, where $\theta_m^l \in [0, 2\pi)$, $m \in \mathcal{M}$, $l \in \mathcal{L}$ is the phase shift by the m -th meta-atom on the l -th transmit metasurface layer. Similarly, for the CSIM, we denote $\Lambda^s = \text{diag}(\lambda^s) \in \mathbb{C}^{N \times N}$, where $\lambda^s = [\lambda_1^s, \dots, \lambda_N^s]^T \in \mathbb{C}^{N \times 1}$. Here, $\lambda_n^s = e^{j\xi_n^s}$ with $\xi_n^s \in [0, 2\pi)$, $n \in \mathcal{N}$, $s \in \mathcal{S}$ being the phase shift by the n -th meta-atom on the s -th CSIM metasurface layer.²

B. Channel Model

The transmission coefficient from the \tilde{m} th meta-atom on the $(l-1)$ st BSIM metasurface layer to the m th meta-atom on the l th BSIM metasurface layer, provided by the Rayleigh-Sommerfeld diffraction theory [19], is written as

$$w_{m,\tilde{m}}^l = \frac{A_t \cos x_{m,\tilde{m}}^l}{r_{m,\tilde{m}}^l} \left(\frac{1}{2\pi r_{m,\tilde{m}}^l} - j \frac{1}{\lambda} \right) e^{j2\pi r_{m,\tilde{m}}^l / \lambda}, l \in \mathcal{L}, \quad (1)$$

where A_t expresses the area of each meta-atom, $x_{m,\tilde{m}}^l$ is the angle between the propagation direction and the normal direction of the $(l-1)$ th BSIM metasurface layer, and $r_{m,\tilde{m}}^l$ is the corresponding transmission distance. As a result, the effect of the BSIM can be modeled as

$$\mathbf{P} = \Phi^L \mathbf{W}^L \dots \Phi^2 \mathbf{W}^2 \Phi^1 \in \mathbb{C}^{M \times M}, \quad (2)$$

where $\mathbf{W}^l \in \mathbb{C}^{M \times M}$, $l \in \mathcal{L}/\{1\}$ is the transmission coefficient matrix between the $(l-1)$ st BSIM metasurface layer and the l th transmit metasurface layer. Regarding $\mathbf{W}^1 \in \mathbb{C}^{M \times M_{\text{BS}}}$, it is the transmission coefficient matrix between the M_{BS} transmit antennas and the first metasurface layer of the BSIM.

In the CSIM, the transmission coefficient from the n th meta-atom on the s th metasurface layer to the \tilde{n} th meta-atom on the $(s-1)$ st metasurface layer can be written as

$$u_{\tilde{n},n}^s = \frac{A_r \cos \zeta_{\tilde{n},n}^s}{t_{\tilde{n},n}^s} \left(\frac{1}{2\pi t_{\tilde{n},n}^s} - j \frac{1}{\lambda} \right) e^{j2\pi t_{\tilde{n},n}^s / \lambda}, s \in \mathcal{S}, \quad (3)$$

where A_r denotes the area of each meta-atom in the CSIM, $\zeta_{\tilde{n},n}^s$ expresses the angle between the propagation direction and

the normal direction of the $(s-1)$ th CSIM metasurface layer, and $t_{\tilde{n},n}^s$ is the corresponding transmission distance. In this case, the effect of the CSIM is described by

$$\mathbf{Z} = \Lambda^S \mathbf{U}^S \dots \Lambda^2 \mathbf{U}^2 \Lambda^1 \in \mathbb{C}^{N \times N}, \quad (4)$$

where $\mathbf{U}^s \in \mathbb{C}^{N \times N}$, $s \in \mathcal{S}/\{1\}$ is the transmission coefficient matrix between the s th CSIM metasurface layer to the $(s-1)$ st CSIM metasurface layer, and $\mathbf{U}^1 \in \mathbb{C}^{N \times 1}$ is the transmission coefficient matrix from the output metasurface layer of the CSIM SIM to user k .

Based on narrowband quasi-static block fading channel modeling, we assume that the duration of each block is τ_c channel uses. Also, by adopting the time-division-duplex (TDD) protocol as the recommended protocol for next-generation systems such as mMIMO systems, τ channel uses are allocated for the uplink training phase and $\tau_c - \tau$ channel uses for the uplink data transmission phase.

Now, we denote $\mathbf{G} = [\mathbf{g}_1 \dots, \mathbf{g}_N] \in \mathbb{C}^{M \times N}$ the channel matrix between the BSIM and the CSIM, where $\mathbf{g}_i \in \mathbb{C}^{M \times 1}$ for $i \in \mathcal{N}$. Moreover, $\mathbf{q}_k \in \mathbb{C}^{N \times 1}$ expresses the channel between the CSIM and user k . Also, we assume the presence of a direct link between the BSIM and user k . We denote the corresponding link as \mathbf{d}_k . In this work, we assume the presence of realistic correlated Rayleigh fading, which occurs in practice [7]. The analysis with correlated Rician fading that includes a line-of-sight (LoS) component could be the topic of future work. Specifically, we have

$$\mathbf{G} = \sqrt{\tilde{\beta}_g} \mathbf{R}_{\text{BSIM}}^{1/2} \mathbf{D} \mathbf{R}_{\text{CSIM}}^{1/2}, \quad (5)$$

$$\mathbf{q}_k = \sqrt{\tilde{\beta}_k} \mathbf{R}_{\text{CSIM}}^{1/2} \mathbf{c}_k, \quad (6)$$

$$\mathbf{d}_k = \sqrt{\tilde{\beta}_k} \mathbf{R}_{\text{BSIM}}^{1/2} \bar{\mathbf{c}}_k, \quad (7)$$

where $\mathbf{R}_{\text{BSIM}} \in \mathbb{C}^{M \times M}$ and $\mathbf{R}_{\text{CSIM}} \in \mathbb{C}^{N \times N}$ describe the correlation matrices at the BSIM and the CSIM respectively. Note that these matrices are deterministic Hermitian-symmetric positive semi-definite and are assumed to be known by the network. The spatial correlation matrices at the BSIM and CSIM are given by [7]

$$[\mathbf{R}_{\text{BSIM}}]_{m,\tilde{m}} = \text{sinc}(2r_{m,\tilde{m}}/\lambda), \tilde{m} \in \mathcal{M}, m \in \mathcal{M}, \quad (8)$$

$$[\mathbf{R}_{\text{CSIM}}]_{\tilde{n},n} = \text{sinc}(2t_{\tilde{n},n}/\lambda), n \in \mathcal{N}, \tilde{n} \in \mathcal{N}, \quad (9)$$

where $r_{m,\tilde{m}}$ and $t_{\tilde{n},n}$ are the corresponding meta-atom spacings. The path-losses $\tilde{\beta}_g$, $\tilde{\beta}_k$, and $\tilde{\beta}_k$ correspond to BSIM-CSIM, CSIM-user k , and BSIM-user k links, while $\mathbf{c}_k \sim \mathcal{CN}(\mathbf{0}, \mathbf{I}_N)$, $\bar{\mathbf{c}}_k \sim \mathcal{CN}(\mathbf{0}, \mathbf{I}_M)$, and $\text{vec}(\mathbf{D}) \sim \mathcal{CN}(\mathbf{0}, \mathbf{I}_{MN})$ represent the small-scale fading parts. Contrary to most previous works, which assume that one of the links of the cascaded channels is deterministic, i.e., it represents a LoS component [8], [24], we consider a more general analysis, since we consider small-scale fading among all links.

By assuming that the phase shift matrices Φ^l , $l \in \mathcal{L}$ and Λ^s , $s \in \mathcal{S}$ are given, the aggregated channel vector from the last BSIM layer to user k , includes the cascaded and direct channels, i.e., $\mathbf{h}_k = \mathbf{G} \mathbf{Z} \mathbf{U}^1 \mathbf{q}_k + \mathbf{d}_k \in \mathbb{C}^{M \times 1}$, which has a covariance matrix given by $\mathbf{R}_k = \mathbb{E}\{\mathbf{h}_k \mathbf{h}_k^H\}$. Specifically, we

¹Without any loss of generality, we assume that the metasurfaces at each SIM include an identical number of meta-atoms.

²We assume that the phase shifts are continuously-adjustable. Also, we assume that the modulus for the coefficient matrices of both SIMs equals to 1 to evaluate the maximization of the achievable rate, e.g., see [5]. The study of more practical designs such as the consideration of coupled phase and magnitude [23] could be the topic of future work.

have

$$\mathbf{R}_k = \hat{\beta}_k \mathbb{E}\{\mathbf{G}\mathbf{Z}\mathbf{U}^1 \mathbb{E}\{\mathbf{q}_k \mathbf{q}_k^H\} \mathbf{U}^{1H} \mathbf{Z}^H \mathbf{G}^H\} + \bar{\beta}_k \mathbf{R}_{\text{BSIM}} \quad (10)$$

$$= \hat{\beta}_k \mathbb{E}\{\mathbf{G}\mathbf{Z}\mathbf{U}^1 \mathbf{R}_{\text{CSIM}} \mathbf{U}^{1H} \mathbf{Z}^H \mathbf{G}^H\} + \bar{\beta}_k \mathbf{R}_{\text{BSIM}} \quad (11)$$

$$= \hat{\beta}_k \text{tr}(\mathbf{R}_{\text{CSIM}} \mathbf{Z} \mathbf{R}_{\text{CSIM}} \mathbf{Z}^H) \mathbf{R}_{\text{BSIM}} + \bar{\beta}_k \mathbf{R}_{\text{BSIM}}, \quad (12)$$

where, in (10), we have applied the independence between \mathbf{G} and \mathbf{q}_k , denoted $\hat{\beta}_k = \hat{\beta}_g \beta_k$, and used $\mathbb{E}\{\mathbf{d}_k \mathbf{d}_k^H\} = \bar{\beta}_k \mathbf{R}_{\text{BSIM}}$. Next, we have used that $\mathbb{E}\{\mathbf{q}_k \mathbf{q}_k^H\} = \bar{\beta}_k \mathbf{R}_{\text{CSIM}}$. In (12), we have denoted $\bar{\mathbf{R}}_{\text{CSIM}} = \mathbf{U}^1 \mathbf{R}_{\text{CSIM}} \mathbf{U}^{1H}$, and we have used the property $\mathbb{E}\{\mathbf{V}\mathbf{U}\mathbf{V}^H\} = \text{tr}(\mathbf{U}) \mathbf{I}_M$, where \mathbf{U} is a deterministic square matrix, and \mathbf{V} is any matrix with independent and identically distributed (i.i.d.) entries of zero mean and unit variance.

III. CHANNEL ESTIMATION AND UPLINK DATA TRANSMISSION

A. Channel Estimation

Given that perfect CSI is not attainable in practice, we employ the TDD protocol that considers an uplink training phase. In this phase, pilot symbols are transmitted to estimate the channel. However, a RIS has the peculiar characteristic that it cannot process any signals, i.e., it cannot obtain receive pilots and it cannot transmit them because it is implemented without any RF chains.

Herein, we propose a channel estimation method, where we estimate the aggregated channel as in [8], [24], [25] instead of the individual channels as in [13], [26], [27]. The latter approach comes with extra power and hardware cost. Moreover, the large dimension BSIM-CSIM channel would require a pilot overhead that would be prohibitively high if we estimated the individual channels. Also, we manage to express the estimated channel in closed form. Hence, the proposed method follows.

During the training phase, which lasts τ channel uses, it is assumed that all users send orthogonal pilot sequences. In particular, $\mathbf{x}_k = [x_{k,1}, \dots, x_{k,\tau}]^H \in \mathbb{C}^{\tau \times 1}$ with $\mathbf{x}_k^H \mathbf{x}_l = 0 \forall k \neq l$ and $\mathbf{x}_k^H \mathbf{x}_k = \tau \rho$ joules denotes the pilot sequence of user k , where all users use the same normalized signal-to-noise ratio (SNR) ρ for transmitting each pilot symbol during the training phase.

Overall, the BS receives

$$\mathbf{Y}^{\text{tr}} = \sum_{i=1}^K \mathbf{W}^{1H} \mathbf{P}^H \mathbf{h}_i \mathbf{x}_i^H + \mathbf{Z}^{\text{tr}}, \quad (13)$$

with $\mathbf{Z}^{\text{tr}} \in \mathbb{C}^{M \times \tau}$ being the received AWGN matrix having independent columns with each one distributed as $\mathcal{CN}(\mathbf{0}, \mathbf{I}_M)$.

By multiplying (13) with \mathbf{x}_k , we obtain

$$\mathbf{r}_k = \mathbf{c}_k + \frac{\mathbf{z}_k}{\tau \rho}, \quad (14)$$

where $\mathbf{c}_k = \mathbf{W}^{1H} \mathbf{P}^H \mathbf{h}_k$ and $\mathbf{z}_k = \mathbf{Z}^{\text{tr}} \mathbf{x}_k$.

Based on linear MMSE estimation, the overall perfect channel can be written as

$$\mathbf{c}_k = \hat{\mathbf{c}}_k + \tilde{\mathbf{c}}_k, \quad (15)$$

where $\hat{\mathbf{c}}_k$ and $\tilde{\mathbf{c}}_k$ are channel estimate and the estimation channel error vectors, respectively. The following lemma

provides the linear MMSE estimated channel. Note that $\hat{\mathbf{c}}_k$ and $\tilde{\mathbf{c}}_k$ are uncorrelated and each of them has zero mean, but they are not independent [28].

Lemma 1: The linear MMSE estimated channel \mathbf{c}_k of user k at the BS is obtained as

$$\hat{\mathbf{c}}_k = \hat{\mathbf{R}}_k \mathbf{Q}_k \mathbf{r}_k, \quad (16)$$

where $\hat{\mathbf{R}}_k = \mathbf{W}^{1H} \mathbf{P}^H \mathbf{R}_k \mathbf{W}^1 \mathbf{P}$, $\mathbf{Q}_k = \left(\hat{\mathbf{R}}_k + \frac{\sigma^2}{\tau \rho} \mathbf{I}_M \right)^{-1}$, and \mathbf{r}_k is the noisy channel given by (14).

Proof: Please see Appendix A. ■

The covariances of $\hat{\mathbf{g}}_k$ and $\tilde{\mathbf{g}}_k$ are easily obtained as

$$\boldsymbol{\Psi}_k = \hat{\mathbf{R}}_k \mathbf{Q}_k \hat{\mathbf{R}}_k, \quad (17)$$

$$\tilde{\boldsymbol{\Psi}}_k = \hat{\mathbf{R}}_k - \boldsymbol{\Psi}_k. \quad (18)$$

As can be seen, in this method, the length of the pilot sequence depends only on the number of users K , and is independent of the number of surfaces and elements at the BSIM and CSIM, which are generally large. Thus, we achieve substantial overhead reduction compared to estimating the individual channel, where the complexity would increase with increasing SIMs sizes. Also, we achieved to obtain the estimated overall channel in closed form instead of works such as [22] that cannot result in analytical expressions.

Another benefit of the proposed two-timescale method is that the channel is required to be estimated when the large-scale statistics (statistical CSI) varies, which is at every several coherence intervals. On the contrary, instantaneous CSI-based approaches would require channel estimation at every coherence interval that would result in high power consumption and computational complexity.

B. Uplink Data Transmission

In this subsection, we provide the derivation of the uplink achievable sum SE of a SIM-assisted mMIMO system.

During the uplink data transmission phase, the BS receives

$$\mathbf{y} = \sqrt{\rho} \sum_{i=1}^K \mathbf{W}^{1H} \mathbf{P}^H \mathbf{h}_i s_i + \mathbf{n}, \quad (19)$$

where $\mathbf{n} \sim \mathcal{CN}(\mathbf{0}, \mathbf{I}_M)$ is the AWGN at the BS, $s_i \sim \mathcal{CN}(0, 1)$ is the transmit signal vector, ρ is the uplink SNR, and \mathbf{h}_i is the aggregated channel from the last BSIM layer to user i .

After application of a receive combining vector \mathbf{v}_k as $\hat{s}_k = \mathbf{v}_k^H \mathbf{y}$, the BS obtains s_k from user k as

$$\begin{aligned} \hat{s}_k &= \sqrt{\rho} \mathbb{E} \left\{ \mathbf{v}_k^H \mathbf{W}^{1H} \mathbf{P}^H \mathbf{h}_k \right\} s_k \\ &+ \sqrt{\rho} \left(\mathbf{v}_k^H \mathbf{W}^{1H} \mathbf{P}^H \mathbf{h}_k - \mathbb{E} \left\{ \mathbf{v}_k^H \mathbf{W}^{1H} \mathbf{P}^H \mathbf{h}_k \right\} \right) s_k \\ &+ \sum_{i \neq k}^K \sqrt{\rho} \mathbf{v}_k^H \mathbf{W}^{1H} \mathbf{P}^H \mathbf{h}_i s_i + \mathbf{v}_k^H \mathbf{n}, \end{aligned} \quad (20)$$

where we have also accounted for channel hardening, which is applicable in mMIMO systems with $M > 8$ [28]. In (20), the first term is the desired signal, the second term is the beamforming gain uncertainty, the third term is multiuser interference, and the last term is the post-processed AWGN noise.

Next, we derive the use-and-then-forget bound on the uplink average SE, which is a lower bound [28]. For this reason, we assume the worst-case uncorrelated additive noise scenario for the inter-user interference and the AWGN noise. In this case, the achievable SE can be written as

$$\text{SE}_k = \frac{\tau_c - \tau}{\tau_c} \log_2(1 + \gamma_k), \quad (21)$$

where the fraction represents the percentage of samples transmitted during the uplink data transmission, and $\gamma_k = \frac{S_k}{I_k}$ denotes the uplink signal-to-interference-plus-noise ratio (SINR). Here, S_k and I_k describe the desired signal power and the interference plus noise power. In terms of \mathbf{g}_k , we have

$$S_k = \rho |\mathbb{E}\{\mathbf{v}_k^H \mathbf{c}_k\}|^2, \quad (22)$$

$$I_k = \mathbb{E}\{|\mathbf{v}_k^H \mathbf{c}_k - \mathbb{E}\{\mathbf{v}_k^H \mathbf{c}_k\}|^2\} + \sum_{i \neq k}^K \mathbb{E}\{|\mathbf{v}_k^H \mathbf{c}_i|^2\} + \mathbb{E}\{|\mathbf{v}_k^H \mathbf{n}|^2\}. \quad (23)$$

In this work, we assume MRC decoding to provide a closed-form SE, i.e., $\mathbf{v}_k = \hat{\mathbf{c}}_k$.³

Theorem 1: The uplink SINR of user k for given SIMs in a BSIM and CSIM assisted mMIMO system is tightly approximated as

$$\gamma_k \approx \frac{S_k}{\tilde{I}_k}, \quad (24)$$

where

$$S_k = \text{tr}^2(\mathbf{\Psi}_k), \quad (25)$$

$$\tilde{I}_k = \sum_{i=1}^K \text{tr}(\hat{\mathbf{R}}_i \mathbf{\Psi}_k) - \text{tr}(\mathbf{\Psi}_k^2) + \frac{1}{\rho} \text{tr}(\mathbf{\Psi}_k). \quad (26)$$

Proof: Please see Appendix B. ■

Theorem 1 provides a tight approximation as the numerical results in Section V reveal. The tightness is also expected because it comes as a result of the exploitation of channel hardening appearing in mMIMO systems [28].

IV. PROBLEM FORMULATION AND OPTIMIZATION

It is crucial to optimize the sum SE in terms of the phase shift matrices of the SIMs included in the proposed architecture.

³The application of the MMSE decoder, which is another common linear receiver used for mMIMO systems due to its better performance, is the topic of ongoing work. The reason is that the corresponding analysis requires the use of deterministic equivalent tools [29]–[31], which result in complicated expressions that would result in an intractable optimization regarding the phase shifts matrices including in BSIM and CSIM.

A. Problem Formulation

By assuming infinite-resolution phase shifters, the formulation of the optimization problem follows as

$$(\mathcal{P}) \quad \max_{\phi_l, \lambda_s} f(\phi_l, \lambda_s) = \sum_{k=1}^K \log_2 \left(1 + \frac{S_k}{\tilde{I}_k} \right) \quad (27a)$$

$$\text{s.t. } \mathbf{P} = \mathbf{\Phi}^L \mathbf{W}^L \dots \mathbf{\Phi}^2 \mathbf{W}^2 \mathbf{\Phi}^1 \mathbf{W}^1, \quad (27b)$$

$$\mathbf{Z} = \mathbf{\Lambda}^K \mathbf{U}^K \dots \mathbf{\Lambda}^2 \mathbf{U}^2 \mathbf{\Lambda}^1 \mathbf{U}^1, \quad (27c)$$

$$\mathbf{\Phi}^l = \text{diag}(\phi_1^l, \dots, \phi_M^l), l \in \mathcal{L}, \quad (27d)$$

$$\mathbf{\Lambda}^s = \text{diag}(\lambda_1^s, \dots, \lambda_N^s), k \in \mathcal{S}, \quad (27e)$$

$$|\phi_m^l| = 1, m \in \mathcal{M}, l \in \mathcal{L}, \quad (27f)$$

$$|\lambda_n^s| = 1, n \in \mathcal{N}, s \in \mathcal{S}. \quad (27g)$$

In problem (\mathcal{P}) , we have denote $f(\phi_l, \lambda_s)$ the objective function that includes the approximate of the SINR provided by Theorem (1).

B. Simultaneous Optimization of Both SIMs

The non-convexity of problem (\mathcal{P}) and the coupling between the optimization variables of the two SIMs, which also have constant modulus constraints lead us to seek a locally optimal solution. Note that many previous optimization methods on RIS-aided systems have applied alternating optimization (AO) to optimize the relevant variables in each case [5], [32]. Although AO-based methods can be implemented easily, their convergence may require many iterations, which increase with increasing the size of RIS [33]. Since SIM-assisted systems are expected to include a large number of elements, the AO methods is not suggested.

Given that the projection operators can be obtained in closed form, we can apply the projected gradient ascent method (PGAM) [34, Ch. 2] for the simultaneous optimization of ϕ_l and λ_s instead of the AO method. Numerical results in Section 64 will demonstrate the superiority of the proposed approach.

C. Proposed Algorithm-PGAM

According to the proposed PGAM, starting from (ϕ_l^0, λ_s^0) , we shift towards the gradient of the objective function, i.e., $\nabla f(\phi_l, \lambda_s)$, where the rate of change of $f(\phi_l, \lambda_s)$ becomes maximum. The newly computed points ϕ_l and λ_s are projected onto Φ_l and Λ_s , respectively to keep the updated points inside the feasible set.

The step size of this shift is determined by a parameter $\mu > 0$. For the sake of description, we define the following sets.

$$\Phi_l = \{\phi_l \in \mathbb{C}^{M \times 1} : |\phi_i^l| = 1, i = 1, \dots, M\}, \quad (28)$$

$$\Lambda_s = \{\lambda_s \in \mathbb{C}^{N \times 1} : |\lambda_i^s| = 1, i = 1, \dots, N\}. \quad (29)$$

The proposed PGAM solving (27) is outlined in Algorithm 1. As can be seen, the algorithm includes the following two iterations.

$$\phi_l^{i+1} = P_{\Phi_l}(\phi_l^i + \mu_i \nabla_{\phi_l} f(\phi_l^i, \lambda_s^i)) \quad (30)$$

$$\lambda_s^{i+1} = P_{\Lambda_s}(\lambda_s^i + \mu_i \nabla_{\lambda_s} f(\phi_l^i, \lambda_s^i)), \quad (31)$$

where $P_{\Phi_l}(\cdot)$ and $P_{\Lambda_s}(\cdot)$ are the projections onto Φ_l and Λ_s , respectively. Also, to find the step size, we apply the Armijo-Goldstein backtracking line search. For this reason, we define the quadratic approximation of $f(\phi_l, \lambda_s)$ as

$$\begin{aligned} Q_\mu(\phi_l, \lambda_s; \mathbf{x}, \mathbf{y}) &= f(\phi_l, \lambda_s) + \langle \nabla_{\phi_l} f(\phi_l, \lambda_s), \mathbf{x} - \phi_l \rangle \\ &\quad - \frac{1}{\mu} \|\mathbf{x} - \phi_l\|_2^2 + \langle \nabla_{\lambda_s} f(\phi_l, \lambda_s), \mathbf{y} - \lambda_s \rangle \\ &\quad - \frac{1}{\mu} \|\mathbf{y} - \lambda_s\|_2^2. \end{aligned} \quad (32)$$

The step size in (30) and (31) can be found as $\mu_i = L_i \kappa^{m_i}$ with $L_i > 0$, and $\kappa \in (0, 1)$, where the parameter m_n is the smallest nonnegative integer satisfying

$$f(\phi_l^{i+1}, \lambda_s^{i+1}) \geq Q_{L_i \kappa^{m_i}}(\phi_l^i, \lambda_s^i; \phi_l^{i+1}, \lambda_s^{i+1}), \quad (33)$$

which can be performed by an iterative procedure.

Algorithm 1 Simultaneous PGAM for both SIMS

```

1: Input:  $\phi_l^0, \lambda_s^0, \mu_1 > 0, \kappa \in (0, 1)$ 
2:  $i \leftarrow 1$ 
3: repeat
4:   repeat
5:      $\phi_l^{i+1} = P_{\Phi_l}(\phi_l^i + \mu_{ni} \nabla_{\phi_l} f(\phi_l^i, \lambda_s^i))$ 
6:      $\lambda_s^{i+1} = P_{\Lambda_s}(\lambda_s^i + \mu_i \nabla_{\lambda_s} f(\phi_l^i, \lambda_s^i))$ 
7:     if  $f(\phi_l^{i+1}, \lambda_s^{i+1}) \leq Q_{\mu_i}(\phi_l^i, \lambda_s^i; \phi_l^{i+1}, \lambda_s^{i+1})$  then
8:        $\mu_i = \mu_i \kappa$ 
9:     end if
10:    until  $f(\phi_l^{i+1}, \lambda_s^{i+1}) > Q_{\mu_i}(\phi_l^i, \lambda_s^i; \phi_l^{i+1}, \lambda_s^{i+1})$ 
11:     $\mu_{i+1} \leftarrow \mu_i$ 
12:     $i \leftarrow i + 1$ 
13:  until convergence
14: Output:  $\phi_l^{i+1}, \lambda_s^{i+1}$ 

```

D. Complex-valued Gradients

Below, we present the gradients $\nabla_{\phi_l} f(\phi_l, \lambda_s)$ and $\nabla_{\lambda_s} f(\phi_l, \lambda_s)$.

Proposition 1: The gradients of $f(\phi_l, \lambda_s)$ regarding ϕ_l^* and λ_s^* are provided closed-forms by

$$\nabla_{\phi_l} f(\phi_l, \lambda_s) = \frac{\tau_c - \tau}{\tau_c \log_2(e)} \sum_{k=1}^K \frac{\tilde{I}_k \nabla_{\phi_l} S_k - S_k \nabla_{\phi_l} \tilde{I}_k}{(1 + \gamma_k) \tilde{I}_k}, \quad (34)$$

$$\nabla_{\lambda_s} f(\phi_l, \lambda_s) = \frac{\tau_c - \tau}{\tau_c \log_2(e)} \sum_{k=1}^K \frac{\tilde{I}_k \nabla_{\lambda_s} S_k - S_k \nabla_{\lambda_s} \tilde{I}_k}{(1 + \gamma_k) \tilde{I}_k}, \quad (35)$$

where

$$\nabla_{\phi_l} S_k = 2 \operatorname{tr}(\Psi_k) \operatorname{diag}(\mathbf{A}_l^H \mathbf{R}_k \mathbf{W}^1 \mathbf{P} \mathbf{B}_k \mathbf{W}^{1H} \mathbf{C}_l^H), \quad (36)$$

$$\begin{aligned} \nabla_{\phi_l} \tilde{I}_k &= \operatorname{diag}(\mathbf{A}_l^H (\mathbf{R}_k \mathbf{W}^1 \mathbf{P} (\Psi + \bar{\Psi}_k \mathbf{B}_k) \\ &\quad + \sum_{i=1}^K \mathbf{R}_i \mathbf{W}^1 \mathbf{P} \mathbf{B}_i) \mathbf{W}^{1H} \mathbf{C}_l^H) \end{aligned} \quad (37)$$

with $\Psi = \sum_{i=1}^K \Psi_i$, $\bar{\Psi}_k = \frac{1}{\rho} \mathbf{I} - 2\Psi_k$, $\mathbf{B}_k = \mathbf{Q}_k \hat{\mathbf{R}}_k - \mathbf{Q}_k \hat{\mathbf{R}}_k^2 \mathbf{Q}_k + \hat{\mathbf{R}}_k \mathbf{Q}_k$, $\mathbf{A}_l = \Phi^L \mathbf{W}^L \dots \Phi^{l+1} \mathbf{W}^{l+1}$, $\mathbf{C}_l =$

$\mathbf{W}^l \Phi^{l-1} \mathbf{W}^{l-1} \dots \Phi^1$, and

$$\begin{aligned} \nabla_{\lambda_s} S_k &= 2 \hat{\beta}_k \operatorname{tr}(\Psi_k) \operatorname{tr}(\mathbf{W}^{1H} \mathbf{P}^H \mathbf{R}_{\text{BSIM}} \mathbf{W}^1 \mathbf{P} \mathbf{B}_k) \\ &\quad \times \operatorname{diag}(\mathbf{F}_s \bar{\mathbf{R}}_{\text{CSIM}} \mathbf{Z}^H \mathbf{R}_{\text{CSIM}} \mathbf{D}_s)^H, \end{aligned} \quad (38)$$

$$\begin{aligned} \nabla_{\lambda_s} \tilde{I}_k &= 2 \operatorname{tr}(\mathbf{W}^{1H} \mathbf{P}^H \mathbf{R}_{\text{BSIM}} \mathbf{W}^1 \mathbf{P} \\ &\quad \times (\sum_{i=1}^K \hat{\beta}_i \hat{\mathbf{R}}_k \mathbf{B}_i + \hat{\beta}_k (\bar{\Psi}_k \mathbf{B}_k + \Psi))) \\ &\quad \times \operatorname{diag}(\mathbf{F}_s \bar{\mathbf{R}}_{\text{CSIM}} \mathbf{Z}^H \mathbf{R}_{\text{CSIM}} \mathbf{D}_s)^H \end{aligned} \quad (39)$$

with $\mathbf{D}_s = \mathbf{U}^{s-1} \Lambda^{s-1} \dots \mathbf{U}^2 \Lambda^1$ and $\mathbf{F}_s = \Lambda^S \mathbf{U}^S \dots \Lambda^{s+1} \mathbf{U}^{s+1}$.

Proof: Please see Appendix C. ■

E. Projection Operations of PGAM

The constraint $|\phi_m^l| = 1$ suggests that ϕ_m^l should be located on the unit circle in the complex plane. Specifically, regarding the vector $\bar{\mathbf{u}}_l$ of $P_{\Phi_l}(\mathbf{u}_l)$, we have

$$\bar{u}_{l,m} = \begin{cases} \frac{u_{l,m}}{|u_{l,m}|} & u_{l,m} \neq 0 \\ e^{j\phi_m^l}, \phi_m^l \in [0, 2\pi] & u_{l,m} = 0 \end{cases}, m = 1, \dots, M, \quad (40)$$

where $\mathbf{u}_l \in \mathbb{C}^{M \times 1}$ is a given point. The projections concerning $|\lambda_s^n| = 1$ follows the same lines.

F. Convergence Analysis

In this section, we start with the presentation of the convergence of Algorithm 1. Specifically, given that the gradients $\nabla_{\phi_l} f(\phi_l, \lambda_s)$ and $\nabla_{\lambda_s} f(\phi_l, \lambda_s)$ are Lipschitz continuous⁴ because they consist of basic functions as shown previously. In this case, we have [34, Chapter 2]

$$\begin{aligned} f(\mathbf{x}, \mathbf{y}) &\geq f(\phi_l, \lambda_s) + \langle \nabla_{\phi_l} f(\phi_l, \lambda_s), \mathbf{x} - \phi_l \rangle \\ &\quad - \frac{1}{L_{\phi_l}} \|\mathbf{x} - \phi_l\|_2^2 + \langle \nabla_{\lambda_s} f(\phi_l, \lambda_s), \mathbf{y} - \lambda_s \rangle - \frac{1}{L_{\lambda_s}} \|\mathbf{y} - \lambda_s\|_2^2 \\ &\geq f(\phi_l, \lambda_s) + \langle \nabla_{\phi_l} f(\phi_l, \lambda_s), \mathbf{x} - \phi_l \rangle \\ &\quad - \frac{1}{L_{\max}} \|\mathbf{x} - \phi_l\|_2^2 + \langle \nabla_{\lambda_s} f(\phi_l, \lambda_s), \mathbf{y} - \lambda_s \rangle \\ &\quad - \frac{1}{L_{\max}} \|\mathbf{y} - \lambda_s\|_2^2, \end{aligned} \quad (42)$$

where $L_{\max} = \max(L_{\phi_l}, L_{\lambda_s})$. Steps 4 – 10 of the algorithm demonstrate its termination in finite iterations because the condition in Step 10 must be fulfilled when $\mu_i < L_{\max}$. The line search results in $f(\phi_l^{i+1}, \lambda_s^{i+1}) \geq f(\phi_l^i, \lambda_s^i)$, which is an increasing sequence of objectives. Given that the sets Φ_l and Λ_s are compact, $f(\phi_l^i, \lambda_s^i)$ converges. It is worthwhile to mention that this is not necessarily an optimal solution because the problem is nonconvex, but a locally optimal solution.

⁴A function $f(\mathbf{x})$ is \mathcal{L} -Lipschitz continuous, or else \mathcal{L} -smooth over a set \mathcal{X} , if for all $\mathbf{x}, \mathbf{y} \in \mathcal{X}$, we have

$$\|\nabla f(\mathbf{y}) - \nabla f(\mathbf{x})\| \leq \mathcal{L} \|\mathbf{y} - \mathbf{x}\|. \quad (41)$$

G. Complexity Analysis

Herein, we elaborate on the complexity (number of complex multiplications) per iteration of the proposed PGAM by using the big- \mathcal{O} notation, which is quite meaningful for large M and N used by the proposed architecture. In particular, for the computation of \mathbf{P} and \mathbf{Z} , we require $(L-1)M^3 + M^2M_{\text{BS}}$ and $(S-1)N^3 + N^2$, multiplications, respectively. The computation of \mathbf{R}_k , which includes a trace over $\mathbf{R}_{\text{CSIM}} \mathbf{Z} \mathbf{R}_{\text{CSIM}} \mathbf{Z}^H$, requires $M^2 + N^2$ multiplications. Note that the former M^2 multiplications are required for the multiplication between the trace and \mathbf{R}_{BSIM} . The complexity of \mathbf{R}_k is $\mathcal{O}(M^3 + M^2)$. From [16], it can be observed that the complexity of Ψ_k , which includes the inverse matrix \mathbf{Q}_k , can be limited to $\mathcal{O}(M^2)$. Hence, the complexity to compute the objective function is $\mathcal{O}(K((L-1)M^3 + (S-1)N^3 + M^2M_{\text{BS}} + N^2))$.

Next, we provide the complexity for the computation of the gradients $\nabla_{\phi_l} f(\phi_l, \lambda_s)$ and $\nabla_{\lambda_s} f(\phi_l, \lambda_s)$. Each of the gradients $\nabla_{\phi_l} S_k$ and $\nabla_{\phi_l} I_k$ require $M^2 + N^2$ multiplications. A similar complexity is exhibited by $\nabla_{\lambda_s} S_k$ and $\nabla_{\phi_l} \tilde{I}_k$. Thus, the total complexity for obtaining the gradients is $\mathcal{O}(K(M^2 + N^2))$.

V. NUMERICAL RESULTS

In this section, we present the evaluation of the achievable sum SE under the proposed algorithm optimizing simultaneously both BSIM and CSIM in terms of analytical results and Monte Carlo simulations.

A. Simulation Setup

We consider the uplink of a BSIM and CSIM-assisted mMIMO system, where the BS, equipped with a uniform linear array (ULA), consists of $M = 64$ antennas that are positioned along the x -axis. The BSIM is integrated with the BS to apply receive beamforming in the EM wave domain. The BSIM is parallel to the $x-y$ plane, and its center aligns with the z -axis at a height $H_{\text{BS}} = 10$ m. The location of the CSIM is at $(x_{\text{CSIM}}, y_{\text{CSIM}}) = (50, 10)$. Also, for the sake of simplicity, we assume that all surfaces are isomorphic and square, which means that the same number of meta-atoms are located along the x - and y -axes, denoted by M_x and M_y , respectively. Note that the spacing between adjacent antennas/meta-atoms for the BS and metasurfaces is assumed to be $\lambda/2$. The size of each meta-atom for both SIMs is $\lambda/2 \times \lambda/2$. Each BS antenna has a gain of 5dBi while each user has a single antenna with a gain of 0dBi [8], [21]. The thickness of both SIMs is $T_{\text{SIM}} = 5\lambda$, while the spacings for the BSIM and CSIM are $d_{\text{BSIM}} = T_{\text{SIM}}/L$ and $d_{\text{CSIM}} = T_{\text{SIM}}/S$, respectively. The users are located on a straight line between $(x_{\text{CSIM}} - \frac{1}{2}d_0, y_{\text{CSIM}} - \frac{1}{2}d_0)$ and $(x_{\text{CSIM}} + \frac{1}{2}d_0, y_{\text{CSIM}} - \frac{1}{2}d_0)$ with equal distances between each two adjacent users, and $d_0 = 20$ m.

The spatial attenuation coefficients $w_{m,\tilde{m}}^l$ and $u_{\tilde{n},n}^s$ between adjacent metasurface layers in BSIM and CSIM are obtained by (1) and (3), respectively. The distance between the \tilde{m} -th meta-atom of the $(l-1)$ -st metasurface and the m -th meta-atom of the l -st metasurface is given by $d_{m,\tilde{m}}^l = \sqrt{d_{\text{BSIM}}^2 + d_{m,\tilde{m}}^2}$,

where

$$d_{m,\tilde{m}} = \frac{\lambda}{2} \sqrt{[|m - \tilde{m}|/M_x]^2 + [\text{mod}(|m - \tilde{m}|, M_x)]^2}. \quad (43)$$

Moreover, the transmission distance between the m -th antenna and the \tilde{m} -th meta-atom on the first metasurface layer is provided by (44). Note that we have $\cos x_{m,\tilde{m}}^l = d_{\text{BSIM}}/d_{m,\tilde{m}}^l, \forall l \in \mathcal{L}$.

Similarly, the distance between the \tilde{n} -th meta-atom of the $(s-1)$ -st metasurface and the n -th meta-atom of the s -st metasurface is given by $d_{n,\tilde{n}}^s = \sqrt{d_{\text{CSIM}}^2 + d_{n,\tilde{n}}^2}$, where

$$d_{n,\tilde{n}} = \frac{\lambda}{2} \sqrt{[|n - \tilde{n}|/N_x]^2 + [\text{mod}(|n - \tilde{n}|, N_x)]^2}. \quad (45)$$

where N_x and N_y are the numbers of meta-atoms along the x - and y -axes of the CSIM.

The path-loss is distance-dependent, and is given by

$$\tilde{\beta}_g = C_0 (d_g/\hat{d})^{-\alpha_g}, \quad (46)$$

where $C_0 = (\lambda_2/4\pi\hat{d})$ is the free space path loss at the reference distance of $\hat{d} = 1$ m, d_g is the distance between the BSIM and the CSIM, and $\alpha_g = 2.5$ is the path-loss exponent. Regarding $\tilde{\beta}_k$ and $\tilde{\beta}_k$, we assume that the corresponding path-loss exponents are equal to 2.8 and 3.5, respectively, while \tilde{d}_k and \tilde{d}_k are the corresponding distances in the place of d_g . The correlation matrices \mathbf{R}_{BSIM} and \mathbf{R}_{CSIM} are calculated according to (8) and (9), respectively. We assume that the carrier frequency and the system bandwidth are 2 GHz and 20 MHz, respectively. The coherence bandwidth is assumed to be $B_c = 200$ KHz, and the coherence interval is $\tau_c = 200$ symbols, given a coherence time equal to $T_c = 1$ ms. Also, we assume $\tau = K$ orthonormal pilot sequences. The uplink SNR for both training and data transmission phases is 6 dB. Furthermore, we assume $M_{\text{BS}} = 32$, $K = 4$, $M = N = 100$, and $L = S = 4$.

B. Convergence of PGAM

In Fig. 2.(a), we show the convergence of the proposed algorithm and its superiority for various sets of meta-atoms per metasurface against the AO method, where the BSIM and CSIM are optimized independently in an alternating way. Termination of the Algorithm 1 takes place when the difference of the objective between the two last iterations is less than 10^{-5} or the number of iterations is larger than 100. We consider three cases, which are $M = N = 100$, $M = 100, N = 49$, and $M = N = 49$. In all cases, the PGAM converges to its maximum as the number of iterations increases. We observe that an increase in the numbers of meta-atoms requires a higher number of iterations for convergence due to expanded search space since now the corresponding matrices are larger. Also, the increases in the numbers of meta-atoms result in higher complexity of Algorithm 1. As M, N increase both methods approach the optimum SE slower. Moreover, it is shown that the PGAM converges quicker to the optimum SE compared to the AO method, which requires more iterations to reach convergence. Note that the SE for the AO is higher at the

$$d_{\tilde{m},m}^1 = \sqrt{d_{\text{BSIM}}^2 + \left[\left(\text{mod}(\tilde{m}-1, M_x) - \frac{M_x-1}{2} \right) \frac{\lambda}{2} - \left(m - \frac{M_{\text{BS}}+1}{2} \right) \frac{\lambda}{2} \right]^2 + \left(\lceil \tilde{m}/M_x \rceil - \frac{M_y+1}{2} \right)^2 \frac{\lambda_2}{4}}. \quad (44)$$

beginning than the PGAM because the starting point for the phase shifts leads to higher SE, while, for the PGAM, the initial rate is a result of the initial values of the phase shifts as described by the algorithm.

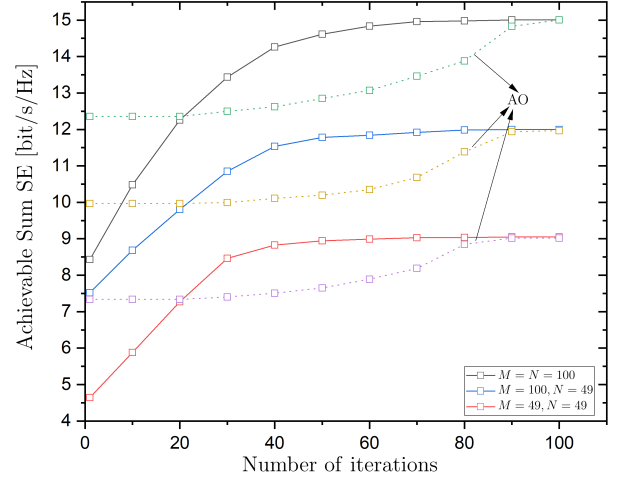
The nonconvexity of Problem (\mathcal{P}) does not allow PGAM to guarantee a stationary solution, which is not necessarily optimal. Hence, Algorithm 1 may converge to different points starting from different initial points. In other words, to mitigate this performance sensitivity of Algorithm 1 on the initial points, it is desirable to select the best solutions after executing the algorithm from different initial points. For this reason, in Fig. 2.(b), we illustrate the sum SE versus the iteration count obtained by Algorithm 1 for 5 different randomly generated initial points. As can be seen, all 5 randomly generated initial points result in the same SE. Generally, it is good to follow this observation and execute Algorithm 1 for 5 randomly generated initial points to allow a good trade-off between performance and complexity.

C. Sum SE Performance Evaluation

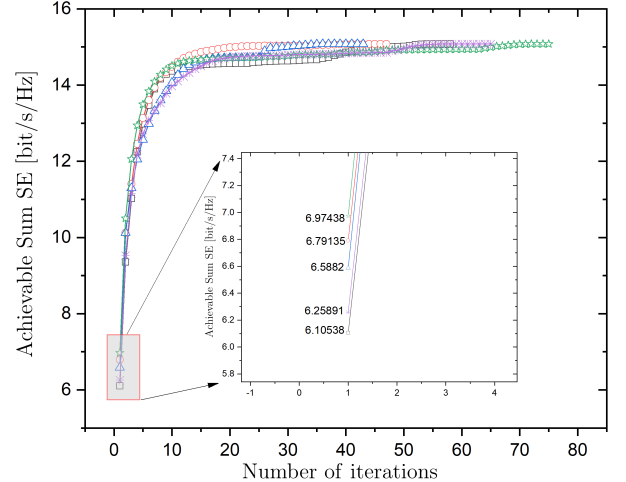
First, Figs. 3.(a) and 3.(b) illustrate the sum SE versus the numbers of meta-atoms M and N on each metasurface layer of the BSIM and CSIM, respectively. In both figures, we observe an increase in the sum SE with the sizes of the corresponding surfaces. However, the impact of the CSIM is greater since a double increase in N results in 170% improvement compared to 200% improvement when M becomes almost double (from 40 to 100). Also, in Fig.3.(b), we observe the impact of the CSIM. In particular, we have shown the SE when the CSIM is absent, and only the direct signal exists, the performance is quite low.

Figs. 4.(a) and 4.(b) depict the sum SE versus the numbers of layers L and S of the BSIM and CSIM, respectively. In Fig. 4.(a), we observe that the sum SE improves until $L = 4$ because of the ability of the BSIM to mitigate the inter-user interference in the EM wave domain. In Fig. 4.(b), it is shown that the sum SE increases with the number of metasurfaces S due to increasing array and multiplexing gains. In both figures, a significant improvement is observed compared to the single-layer BSIM and CSIM, respectively. However, this improvement in the BSIM is greater.

In Fig. 7, we show the sum SE versus the number of users K . We observe that the sum SE grows with K at the beginning but decreases after a certain value of K . The reason behind this observation is that the increase in the beginning comes from the increase of the spatial multiplexing gain with K . Later, the increase of inter-user interference due to increasing K cannot be mitigated by the BSIM and its wave-based decoding. Based on our setup, the BSIM can mitigate the multiuser interference of maximum $K = 5$ users. Moreover, we observe that an increase in the number of meta-atoms M of the BSIM can serve a larger number of users.



(a) Achievable sum SE of the proposed double-SIM mMIMO architecture versus the number of iterations for various sets of numbers meta-atoms per metasurface.

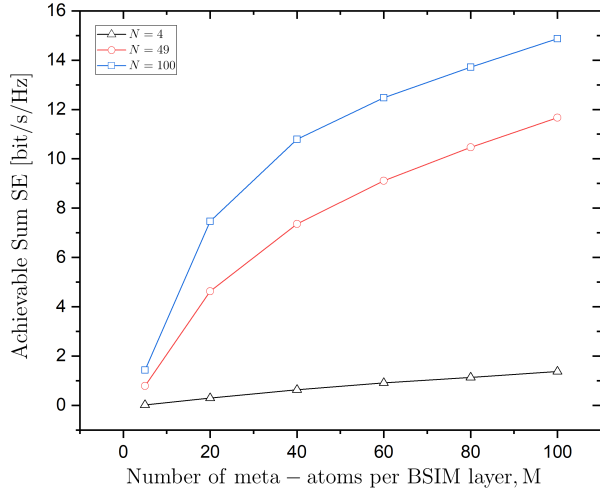


(b) Achievable sum SE of the proposed double-SIM mMIMO architecture versus the number of iterations for 5 different randomly generated initial points.

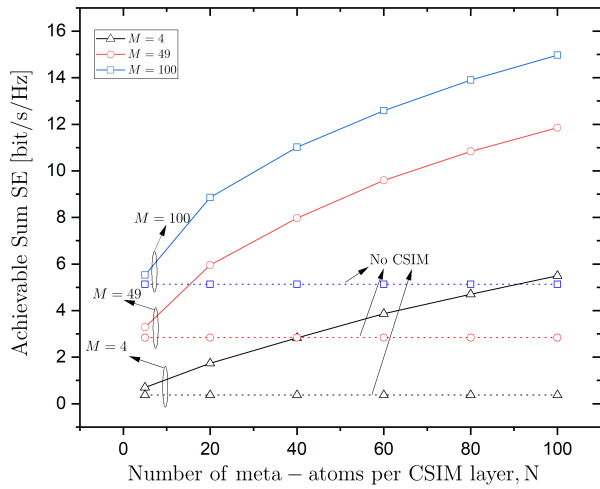
Fig. 2

Fig. 6 depicts the sum SE versus the transmit SNR for various cases regarding the values of the phase shifts of the BSIM. The optimal phase shifts design achieves the best performance as expected. The designs with random phase shifts and equal phase shifts follow with lower performance. In parallel, Monte Carlo simulations verify the analytical results.

In Fig. 7, we present a comparison between the BCIM and CSIM-assisted mMIMO system with the case where the BSIM is replaced by a conventional BS that employs a conventional zero-forcing (ZF) decoder for mitigating the multiuser interference. For the sake of a fair comparison,



(a) Achievable sum SE of the proposed double-SIM mMIMO architecture versus the number of meta-atoms of the BSIM M while varying the number of meta-atoms of the CSIM N .



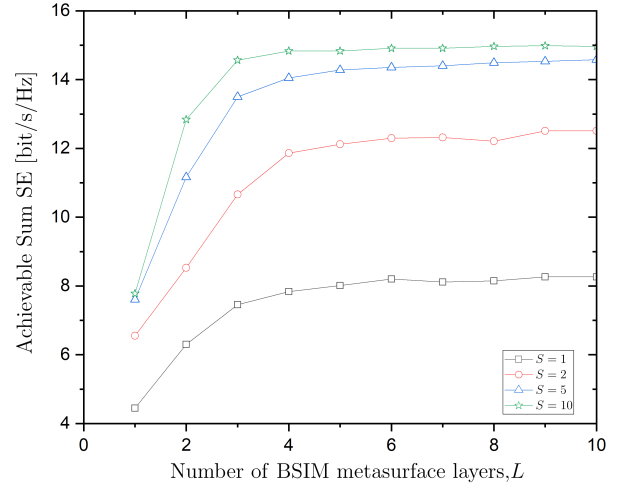
(b) Achievable sum SE of the proposed double-SIM mMIMO architecture versus the number of meta-atoms of the CSIM N while varying the number of meta-atoms of the BSIM M .

Fig. 3

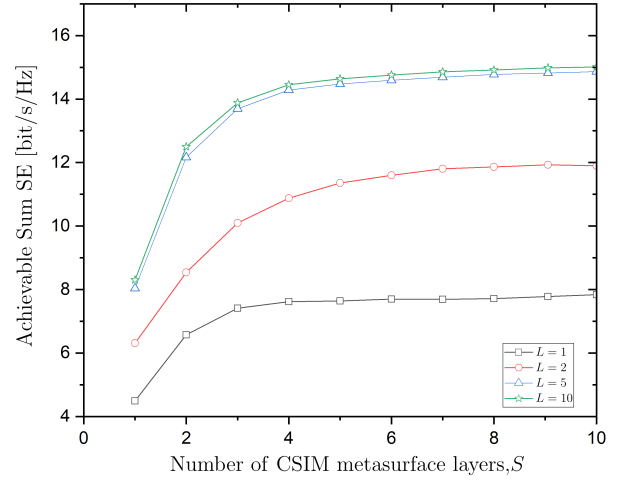
we assume that the path loss corresponding to user k is $d_k = \sqrt{H_{BS}^2 + (d_0(k-1))^2}$. The conventional BS requires $M_{BS} = 16$ antennas to exhibit better performance than the BSIM with $M_{BS} = 64$ and $M = 49$ elements. In other words, we can remove completely the digital decoding at the BS while equipping each antenna with low-resolution ADCs/DACs that can reduce overall the energy consumption and hardware cost.

VI. CONCLUSION

In this paper, a novel SIM-assisted mMIMO architecture was proposed. In particular, a SIM enables wave-based decoding in the uplink, and another SIM is used at the intermediate space between the users and the BS to increase further the ability of the proposed configuration to reshape the surrounding EM environment. We first suggested a channel estimation scheme, which obtains the estimated channel in closed form in a single



(a) Achievable sum SE of the proposed double-SIM mMIMO architecture versus the number of metasurfaces of the BSIM L while varying the number of metasurfaces of the CSIM S .



(b) Achievable sum SE of the proposed double-SIM mMIMO architecture versus the number of metasurfaces of the CSIM S while varying the number of metasurfaces of the BSIM L .

Fig. 4

phase. Then, we derived the uplink sum SE, and optimized both SIMs simultaneously. Simulations showed the superiority of the proposed architecture compared to counterparts, demonstrated the impact of various parameters on the sum SE, and exhibited outperformance against the AO method, where the SIMs are optimized separately. For example, an increase in the numbers of layers and meta-atoms increases the performance. Especially, the BSIM exhibits interference cancellation. Also, the proposed architecture is superior to the conventional digital MISO counterpart, which means that SIM-based designs could lead to next-generation energy-efficient networks.

APPENDIX A PROOF OF LEMMA 1

The LMMSE estimator of $\mathbf{c}_k = \mathbf{W}^H \mathbf{P}^H \mathbf{h}_k$ is derived according to according to [35, Ch. 12] as

$$\hat{\mathbf{c}}_k = \mathbb{E}\{\mathbf{r}_k \mathbf{g}_k^H\} (\mathbb{E}\{\mathbf{r}_k \mathbf{r}_k^H\})^{-1}. \quad (47)$$

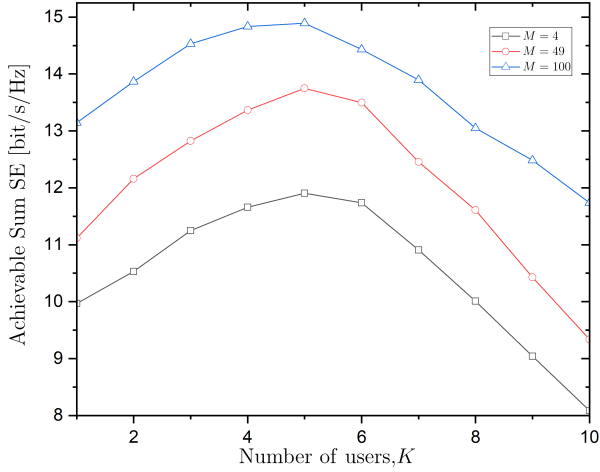


Fig. 5: Achievable sum SE of the proposed double-SIM mMIMO architecture versus the number of users K while varying the number of BCSIM meta-atoms M .

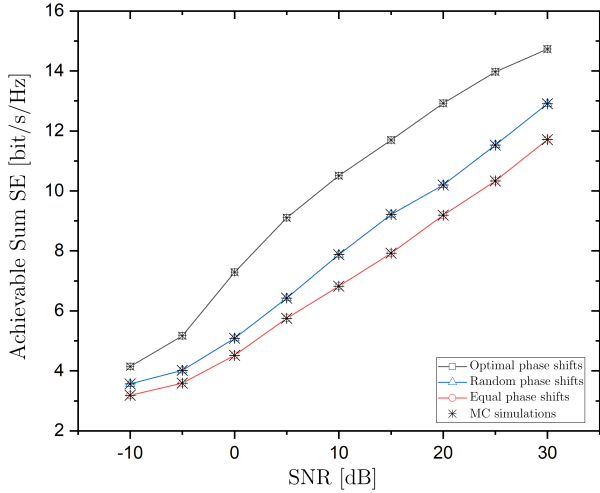


Fig. 6: Achievable sum SE of the proposed double-SIM mMIMO architecture versus the SNR for different cases regarding the phase shifts.

The first term of (47) is written as

$$\mathbb{E}\{\mathbf{r}_k \mathbf{c}_k^H\} = \mathbb{E}\left[\left(\mathbf{W}^H \mathbf{P}^H \mathbf{c}_k + \frac{\mathbf{z}_k}{\tau\rho}\right) \mathbf{c}_k^H \mathbf{W}^1 \mathbf{P}\right] \quad (48)$$

$$= \mathbf{W}^H \mathbf{P}^H \mathbb{E}\{\mathbf{c}_k \mathbf{c}_k^H\} \mathbf{W}^1 \mathbf{P} = \mathbf{W}^H \mathbf{P}^H \mathbf{R}_k \mathbf{W}^1 \mathbf{P}. \quad (49)$$

The second term is obtained as

$$\mathbb{E}\{\mathbf{r}_k \mathbf{r}_k^H\} = \mathbf{W}^H \mathbf{P}^H \mathbf{R}_k \mathbf{W}^1 \mathbf{P} + \frac{\sigma^2}{\tau\rho} \mathbf{I}_M. \quad (50)$$

By inserting (49) and (50) into (47), we obtain

$$\hat{\mathbf{c}}_k = \hat{\mathbf{R}}_k \mathbf{Q}_k \mathbf{r}_k, \quad (51)$$

where $\hat{\mathbf{R}}_k = \mathbf{W}^H \mathbf{P}^H \mathbf{R}_k \mathbf{W}^1 \mathbf{P}$ and $\mathbf{Q}_k = \left(\hat{\mathbf{R}}_k + \frac{\sigma^2}{\tau\rho} \mathbf{I}_M\right)^{-1}$.

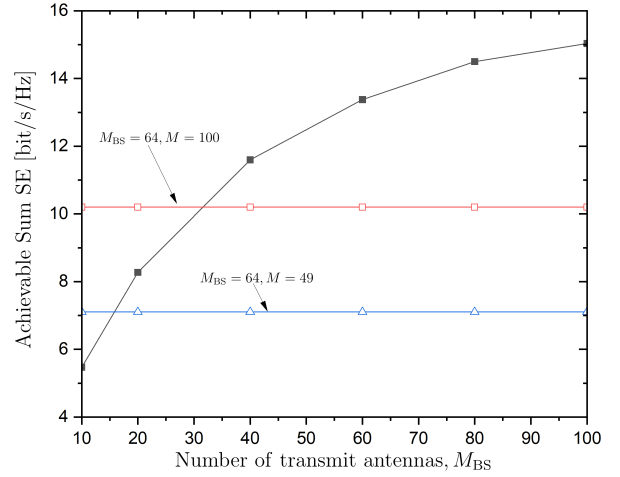


Fig. 7: Achievable sum SE of the proposed double-SIM mMIMO architecture versus the number of BS antennas M_{BS} while varying the number of receiver metasurface layers K .

APPENDIX B PROOF OF THEOREM 1

Regarding the desired signal power part, we have

$$\begin{aligned} \mathbb{E}\{\mathbf{v}_k^H \mathbf{c}_k\} &= \text{tr}(\mathbb{E}\{\mathbf{c}_k \hat{\mathbf{c}}_k\}) \\ &= \text{tr}(\mathbb{E}\{\mathbf{c}_k \hat{\mathbf{R}}_k \mathbf{Q}_k \mathbf{r}_k\}) \end{aligned} \quad (52)$$

$$= \text{tr}(\mathbf{\Psi}_k), \quad (53)$$

where, in (52), we have inserted (20), while in the last equation, we have computed the expectation between \mathbf{c}_k and \mathbf{r}_k , and we have used (17).

In the case of I_k , the first term can be written as

$$\mathbb{E}\{|\hat{\mathbf{c}}_k^H \mathbf{c}_k - \mathbb{E}\{\hat{\mathbf{c}}_k^H \mathbf{c}_k\}|^2\} = \mathbb{E}\{|\hat{\mathbf{c}}_k^H \mathbf{c}_k|^2\} - |\mathbb{E}\{\hat{\mathbf{c}}_k^H \mathbf{c}_k\}|^2 \quad (54)$$

$$= \mathbb{E}\{|\hat{\mathbf{c}}_k^H \hat{\mathbf{c}}_k + \hat{\mathbf{c}}_k^H \tilde{\mathbf{c}}_k|^2\} - |\mathbb{E}\{\hat{\mathbf{c}}_k^H \hat{\mathbf{c}}_k\}|^2 \quad (55)$$

$$= \mathbb{E}\{|\hat{\mathbf{c}}_k^H \tilde{\mathbf{c}}_k|^2\} + 2 \text{Re}\{\mathbb{E}\{\hat{\mathbf{c}}_k^H \tilde{\mathbf{c}}_k \hat{\mathbf{c}}_k^H \tilde{\mathbf{c}}_k\}\} \quad (56)$$

where in (55), we have substituted (15). The second term in (56) goes to zero according to the channel hardening property in mMIMO, which gives with high accuracy $\hat{\mathbf{c}}_k^H \tilde{\mathbf{c}}_k \approx \mathbb{E}\{\hat{\mathbf{c}}_k^H \tilde{\mathbf{c}}_k\}$ [28]. Specifically, the second term becomes

$$\mathbb{E}\{\hat{\mathbf{c}}_k^H \tilde{\mathbf{c}}_k \hat{\mathbf{c}}_k^H \tilde{\mathbf{c}}_k\} \approx \mathbb{E}\{\hat{\mathbf{c}}_k^H \tilde{\mathbf{c}}_k\} \mathbb{E}\{\hat{\mathbf{c}}_k^H \tilde{\mathbf{c}}_k\} = 0. \quad (57)$$

Hence, (56) becomes

$$\mathbb{E}\{|\hat{\mathbf{c}}_k^H \mathbf{c}_k - \mathbb{E}\{\hat{\mathbf{c}}_k^H \mathbf{c}_k\}|^2\} \approx \mathbb{E}\{|\hat{\mathbf{c}}_k^H \tilde{\mathbf{c}}_k|^2\} \quad (58)$$

$$= \text{tr}(\hat{\mathbf{R}}_k \mathbf{\Psi}_k) - \text{tr}(\mathbf{\Psi}_k^2). \quad (59)$$

For the derivation of (59), we apply the approximations $\hat{\mathbf{c}}_k^H \tilde{\mathbf{c}}_k \approx \mathbb{E}\{\hat{\mathbf{c}}_k^H \tilde{\mathbf{c}}_k\}$ and $\tilde{\mathbf{c}}_k^H \tilde{\mathbf{c}}_k \approx \mathbb{E}\{\tilde{\mathbf{c}}_k^H \tilde{\mathbf{c}}_k\}$ due to channel hardening. Thus, we result in

$$\mathbb{E}\{|\hat{\mathbf{c}}_k^H \tilde{\mathbf{c}}_k|^2\} = \text{tr}(\mathbb{E}\{\hat{\mathbf{c}}_k \hat{\mathbf{c}}_k^H \tilde{\mathbf{c}}_k \tilde{\mathbf{c}}_k^H\}) \quad (60)$$

$$\approx \text{tr}(\mathbb{E}\{\hat{\mathbf{c}}_k \hat{\mathbf{c}}_k^H\} \mathbb{E}\{\tilde{\mathbf{c}}_k \tilde{\mathbf{c}}_k^H\}) \quad (61)$$

$$= \text{tr}((\hat{\mathbf{R}}_k - \mathbf{\Psi}_k) \mathbf{\Psi}_k). \quad (62)$$

The multiuser interference term in (23) becomes

$$\mathbb{E}\{|\hat{\mathbf{c}}_k^H \mathbf{c}_i|^2\} = \mathbb{E}\{|\hat{\mathbf{c}}_k^H(\hat{\mathbf{c}}_i + \tilde{\mathbf{c}}_i)|^2\} \quad (63)$$

$$= \mathbb{E}\{|\hat{\mathbf{c}}_k^H \hat{\mathbf{c}}_i|^2\} + \mathbb{E}\{|\hat{\mathbf{c}}_k^H \tilde{\mathbf{c}}_i|^2\} + 2 \operatorname{Re}\{\mathbb{E}\{\hat{\mathbf{c}}_k^H \hat{\mathbf{c}}_i \tilde{\mathbf{c}}_i^H \hat{\mathbf{c}}_k\}\} \quad (64)$$

$$= \operatorname{tr}(\Psi_k \hat{\mathbf{R}}_i), \quad (65)$$

where the third term in (65) is zero because it holds that

$$2 \operatorname{Re}\{\mathbb{E}\{\hat{\mathbf{c}}_k^H \hat{\mathbf{c}}_i \tilde{\mathbf{c}}_i^H \hat{\mathbf{c}}_k\}\} = 2 \operatorname{Re}\{\mathbb{E}\{\operatorname{tr}((\hat{\mathbf{c}}_k \hat{\mathbf{c}}_k^H)(\tilde{\mathbf{c}}_i \hat{\mathbf{c}}_i^H))\}\} \quad (66)$$

$$= 2 \operatorname{Re}\{\operatorname{tr}(\mathbb{E}\{\hat{\mathbf{c}}_k \hat{\mathbf{c}}_k^H\} \mathbb{E}\{\tilde{\mathbf{c}}_i \hat{\mathbf{c}}_i^H\})\} \quad (67)$$

$$= 0, \quad (68)$$

where, first, we used that $\hat{\mathbf{c}}_k$ and $\hat{\mathbf{c}}_i$ are independent, and next that $\tilde{\mathbf{c}}_i$ and $\hat{\mathbf{c}}_i$ are uncorrelated.

The last term in (23) is written as

$$\mathbb{E}\{|\hat{\mathbf{c}}_k^H \mathbf{n}|^2\} = \operatorname{tr}(\mathbb{E}\{\hat{\mathbf{c}}_k \hat{\mathbf{c}}_k^H\}) \quad (69)$$

$$= \operatorname{tr}(\Psi_k), \quad (70)$$

where, in (69), we have used that $\hat{\mathbf{c}}_k$ and \mathbf{n} are uncorrelated.

The combination of (59), (65), and (69) provides the approximate of I_k , which is \tilde{I}_k , and concludes the proof.

APPENDIX C PROOF OF PROPOSITION 1

First, we focus on the derivation of $\nabla_{\phi_l} f(\phi_l, \lambda_s)$. From (27a), we can easily obtain

$$\nabla_{\phi_l} f(\phi_l, \lambda_s) = \frac{\tau_c - \tau}{\tau_c \log_2(e)} \sum_{k=1}^K \frac{\tilde{I}_k \nabla_{\phi_l} S_k - S_k \nabla_{\phi_l} \tilde{I}_k}{(1 + \gamma_k) \tilde{I}_k}. \quad (71)$$

For the computation of $\nabla_{\phi_l} S_k$, we obtain its differential as

$$\begin{aligned} d(S_k) &= d(\operatorname{tr}(\Psi_k)^2) \\ &= 2 \operatorname{tr}(\Psi_k) d \operatorname{tr}(\Psi_k) \\ &= 2 \operatorname{tr}(\Psi_k) \operatorname{tr}(d\Psi_k). \end{aligned} \quad (72)$$

Application of [36, Eq. (3.35)] gives

$$\begin{aligned} d(\Psi_k) &= d(\hat{\mathbf{R}}_k \mathbf{Q}_k \hat{\mathbf{R}}_k) \\ &= d(\hat{\mathbf{R}}_k) \mathbf{Q}_k \hat{\mathbf{R}}_k + \hat{\mathbf{R}}_k d(\mathbf{Q}_k) \hat{\mathbf{R}}_k + \hat{\mathbf{R}}_k \mathbf{Q}_k d(\hat{\mathbf{R}}_k). \end{aligned} \quad (73)$$

To this end, we have to derive $d(\hat{\mathbf{R}}_k)$ and $d(\mathbf{Q}_k)$. The former can be written as

$$d(\hat{\mathbf{R}}_k) = \mathbf{W}^{1H} d(\mathbf{P}^H) \mathbf{R}_k \mathbf{W}^1 \mathbf{P} + \mathbf{W}^{1H} \mathbf{P}^H \mathbf{R}_k \mathbf{W}^1 d(\mathbf{P}). \quad (74)$$

The latter is derived based on [36, eqn. (3.40)] as

$$\begin{aligned} d(\mathbf{Q}_k) &= d(\hat{\mathbf{R}}_k + \frac{\sigma}{\tau P} \mathbf{I}_M)^{-1} \\ &= -(\hat{\mathbf{R}}_k + \frac{\sigma^2}{\tau P} \mathbf{I}_M)^{-1} d(\hat{\mathbf{R}}_k + \frac{\sigma^2}{\tau P} \mathbf{I}_M) (\hat{\mathbf{R}}_k + \frac{\sigma}{\tau P} \mathbf{I}_M)^{-1} \\ &= -\mathbf{Q}_k d(\hat{\mathbf{R}}_k) \mathbf{Q}_k. \end{aligned} \quad (75)$$

Substitution of (74) and (75) into (73) allows to obtain $d(S_k)$ from (72) as

$$\begin{aligned} d(S_k) &= 2 \operatorname{tr}(\Psi_k) \operatorname{tr}(\mathbf{A}_l^H \mathbf{R}_k \mathbf{W}^1 \mathbf{P} \mathbf{B}_k \mathbf{W}^{1H} \mathbf{C}_l^H d(\Phi^{1H}) \\ &\quad + \mathbf{C}_l \mathbf{B}_k \mathbf{W}^{1H} \mathbf{P}^H \mathbf{R}_k \mathbf{W}^1 \mathbf{A}_l d(\Phi^1)) \end{aligned} \quad (76)$$

$$\begin{aligned} &= 2 \operatorname{tr}(\Psi_k) \left(\operatorname{diag}(\mathbf{A}_l^H \mathbf{R}_k \mathbf{W}^1 \mathbf{P} \mathbf{B}_k \mathbf{W}^{1H} \mathbf{C}_l^H) \right)^T d(\phi^{1*}) \\ &\quad + \left(\operatorname{diag}(\mathbf{C}_l \mathbf{B}_k \mathbf{W}^{1H} \mathbf{P}^H \mathbf{R}_k \mathbf{W}^1 \mathbf{A}_l) \right)^T d(\phi^1), \end{aligned} \quad (77)$$

where $\mathbf{B}_k = \mathbf{Q}_k \hat{\mathbf{R}}_k - \mathbf{Q}_k \hat{\mathbf{R}}_k^2 \mathbf{Q}_k + \hat{\mathbf{R}}_k \mathbf{Q}_k$, $\mathbf{A}_l = \Phi^L \mathbf{W}^L \dots \Phi^{l+1} \mathbf{W}^{l+1}$, and $\mathbf{C}_l = \mathbf{W}^l \Phi^{l-1} \mathbf{W}^{l-1} \dots \Phi^1$. In (76), we have also used (2) by writing its differential as $d(\mathbf{P}) = \mathbf{A}_l \Phi_l \mathbf{C}_l$

It can be easily obtained from (77) that

$$\begin{aligned} \nabla_{\phi_l} S_k &= 2 \operatorname{tr}(\Psi_k) \\ &\quad \times \frac{\partial}{\partial(\phi_l^*)} \left(\left(\operatorname{diag}(\mathbf{A}_l^H \mathbf{R}_k \mathbf{W}^1 \mathbf{P} \mathbf{B}_k \mathbf{W}^{1H} \mathbf{C}_l^H) \right)^T d(\phi_l^*) \right. \\ &\quad \left. + \left(\mathbf{C}_l \mathbf{B}_k \mathbf{W}^{1H} \mathbf{P}^H \mathbf{R}_k \mathbf{W}^1 \mathbf{A}_l \right)^T d(\phi_l) \right) \\ &= 2 \operatorname{tr}(\Psi_k) \operatorname{diag}(\mathbf{A}_l^H \mathbf{R}_k \mathbf{W}^1 \mathbf{P} \mathbf{B}_k \mathbf{W}^{1H} \mathbf{C}_l^H). \end{aligned} \quad (78)$$

Regarding $\nabla_{\phi_l} \tilde{I}_k$, we obtain the differential from (26) as

$$d(\tilde{I}_k) = \operatorname{tr}(\Psi d(\hat{\mathbf{R}}_k)) + \sum_{i=1}^K \operatorname{tr}(\hat{\mathbf{R}}_k d(\Psi_i)) + \operatorname{tr}(\bar{\Psi}_k d(\Psi_k)), \quad (79)$$

where $\Psi = \sum_{i=1}^K \Psi_i$, $\bar{\Psi}_k = \frac{1}{\rho} \mathbf{I} - 2\Psi_k$. Having obtained the differentials in (79) previously and after several algebraic manipulations, we obtain

$$\begin{aligned} \nabla_{\phi_l} \tilde{I}_k &= \frac{\partial}{\partial \phi_l^*} \tilde{I}_k \\ &= \operatorname{diag}(\mathbf{A}_l^H (\mathbf{R}_k \mathbf{W}^1 \mathbf{P} (\Psi + \bar{\Psi}_k \mathbf{B}_k) \\ &\quad + \sum_{i=1}^K \mathbf{R}_i \mathbf{W}^1 \mathbf{P} \mathbf{B}_i) \mathbf{W}^{1H} \mathbf{C}_l^H). \end{aligned} \quad (80)$$

In the case of $\nabla_{\lambda_s} f(\phi_l, \lambda_s)$, we obtain similar expressions, but now $d(\hat{\mathbf{R}}_k)$ is derived as

$$\begin{aligned} d(\hat{\mathbf{R}}_k) &= \mathbf{W}^{1H} \mathbf{P}^H d(\mathbf{R}_k) \mathbf{W}^1 \mathbf{P} \\ &= \hat{\beta}_k \mathbf{W}^{1H} \mathbf{P}^H \operatorname{tr}(\mathbf{R}_{\text{CSIM}} d(\mathbf{Z}) \bar{\mathbf{R}}_{\text{CSIM}} \mathbf{Z}^H \\ &\quad + \mathbf{R}_{\text{CSIM}} \bar{\mathbf{Z}} \bar{\mathbf{R}}_{\text{CSIM}} d(\mathbf{Z}^H)) \mathbf{R}_{\text{BSIM}} \mathbf{W}^1 \mathbf{P} \\ &= \hat{\beta}_k \mathbf{W}^{1H} \mathbf{P}^H \operatorname{tr}(\mathbf{F}_s \bar{\mathbf{R}}_{\text{CSIM}} \mathbf{Z}^H \mathbf{R}_{\text{CSIM}} \mathbf{D}_s d(\Lambda_s) \\ &\quad + (\mathbf{F}_s \bar{\mathbf{R}}_{\text{CSIM}} \mathbf{Z}^H \mathbf{R}_{\text{CSIM}} \mathbf{D}_s)^H d(\Lambda_s^H)) \mathbf{R}_{\text{BSIM}} \mathbf{W}^1 \mathbf{P}, \end{aligned} \quad (81)$$

where, in (81), we have substituted (12). We have also denoted $\mathbf{D}_s = \mathbf{U}^{s-1} \Lambda^{s-1} \dots \mathbf{U}^2 \Lambda^1$ and $\mathbf{F}_s = \Lambda^S \mathbf{U}^S \dots \Lambda^{s+1} \mathbf{U}^{s+1}$. In (83), we have used (4) by writing its differential as $d(\mathbf{Z}) = \mathbf{D}_s \Lambda_s \mathbf{F}_s$.

Substitution of (83) and (75) into (73) allows to obtain $d(S_k)$ from (72) as

$$\begin{aligned} d(S_k) &= 2 \hat{\beta}_k \operatorname{tr}(\Psi_k) \operatorname{tr}(\mathbf{W}^{1H} \mathbf{P}^H \mathbf{R}_{\text{BSIM}} \mathbf{W}^1 \mathbf{P} \mathbf{B}_k) \\ &\quad \times \left(\operatorname{diag}(\mathbf{F}_s \bar{\mathbf{R}}_{\text{CSIM}} \mathbf{Z}^H \mathbf{R}_{\text{CSIM}} \mathbf{D}_s)^H \right)^T d(\lambda_s^*) \\ &\quad + \left(\operatorname{diag}(\mathbf{F}_s \bar{\mathbf{R}}_{\text{CSIM}} \mathbf{Z}^H \mathbf{R}_{\text{CSIM}} \mathbf{D}_s) \right)^T d(\lambda_s). \end{aligned} \quad (84)$$

Thus, we obtain

$$\begin{aligned} \nabla_{\lambda_s} S_k &= 2\hat{\beta}_k \text{tr}(\Psi_k) \text{tr}\left(\mathbf{W}^{1H} \mathbf{P}^H \mathbf{R}_{\text{BSIM}} \mathbf{W}^1 \mathbf{P} \mathbf{B}_k\right) \\ &\times \text{diag}(\mathbf{F}_s \bar{\mathbf{R}}_{\text{CSIM}} \mathbf{Z}^H \mathbf{R}_{\text{CSIM}} \mathbf{D}_s)^H. \end{aligned} \quad (85)$$

Similar to (81), we obtain from (79) and (83) and after some algebraic manipulations

$$\begin{aligned} \nabla_{\lambda_s} \tilde{I}_k &= 2 \text{tr}\left(\mathbf{W}^{1H} \mathbf{P}^H \mathbf{R}_{\text{BSIM}} \mathbf{W}^1 \mathbf{P}\right) \\ &\times \left(\sum_{i=1}^K \hat{\beta}_i \hat{\mathbf{R}}_k \mathbf{B}_i + \hat{\beta}_k (\bar{\Psi}_k \mathbf{B}_k + \Psi)\right) \\ &\times \text{diag}(\mathbf{F}_s \bar{\mathbf{R}}_{\text{CSIM}} \mathbf{Z}^H \mathbf{R}_{\text{CSIM}} \mathbf{D}_s)^H, \end{aligned} \quad (86)$$

which concludes the proof.

REFERENCES

- [1] F. Boccardi *et al.*, “Five disruptive technology directions for 5G,” *IEEE Commun. Mag.*, vol. 52, no. 2, pp. 74–80, 2014.
- [2] J. Zhang *et al.*, “Prospective multiple antenna technologies for beyond 5G,” *IEEE J. Sel. Areas Commun.*, vol. 38, no. 8, pp. 1637–1660, 2020.
- [3] F. Sahrabi and W. Yu, “Hybrid digital and analog beamforming design for large-scale antenna arrays,” *IEEE J. Sel. Top. Signal Proc.*, vol. 10, no. 3, pp. 501–513, 2016.
- [4] T. S. Rappaport *et al.*, “Wideband millimeter-wave propagation measurements and channel models for future wireless communication system design,” *IEEE Trans. Commun.*, vol. 63, no. 9, pp. 3029–3056, 2015.
- [5] Q. Wu and R. Zhang, “Intelligent reflecting surface enhanced wireless network via joint active and passive beamforming,” *IEEE Trans. Wireless Commun.*, vol. 18, no. 11, pp. 5394–5409, 2019.
- [6] E. Basar *et al.*, “Wireless communications through reconfigurable intelligent surfaces,” *IEEE Access*, vol. 7, pp. 116 753–116 773, 2019.
- [7] E. Björnson and L. Sanguinetti, “Rayleigh fading modeling and channel hardening for reconfigurable intelligent surfaces,” *IEEE Wireless Commun. Lett.*, vol. 10, no. 4, pp. 830–834, 2021.
- [8] A. Papazafeiropoulos *et al.*, “Intelligent reflecting surface-assisted MU-MISO systems with imperfect hardware: Channel estimation and beamforming design,” *IEEE Trans. Wireless Commun.*, vol. 21, no. 3, pp. 2077–2092, 2021.
- [9] A. Papazafeiropoulos, “Ergodic capacity of IRS-assisted MIMO systems with correlation and practical phase-shift modeling,” *IEEE Wireless Commun. Lett.*, vol. 11, no. 2, pp. 421–425, 2022.
- [10] C. Huang *et al.*, “Reconfigurable intelligent surfaces for energy efficiency in wireless communication,” *IEEE Trans. Wireless Commun.*, vol. 18, no. 8, pp. 4157–4170, 2019.
- [11] M. Di Renzo *et al.*, “Smart radio environments empowered by reconfigurable intelligent surfaces: How it works, state of research, and the road ahead,” *IEEE J. Sel. Areas Commun.*, vol. 38, no. 11, pp. 2450–2525, 2020.
- [12] Q. U. A. Nadeem *et al.*, “Asymptotic max-min SINR analysis of reconfigurable intelligent surface assisted MISO systems,” *IEEE Trans. Wireless Commun.*, vol. 19, no. 12, pp. 7748–7764, 2020.
- [13] Y. Yang *et al.*, “Intelligent reflecting surface meets OFDM: Protocol design and rate maximization,” *IEEE Trans. Commun.*, vol. 68, no. 7, pp. 4522–4535, 2020.
- [14] C. Pan *et al.*, “Multicell MIMO communications relying on intelligent reflecting surfaces,” *IEEE Trans. Wireless Commun.*, vol. 19, no. 8, pp. 5218–5233, 2020.
- [15] A. Papazafeiropoulos *et al.*, “Coverage probability of distributed IRS systems under spatially correlated channels,” *IEEE Wireless Commun. Lett.*, vol. 10, no. 8, pp. 1722–1726, 2021.
- [16] —, “Achievable rate of a STAR-RIS assisted massive MIMO system under spatially-correlated channels,” *IEEE Trans. Wireless Commun.*, pp. 1–1, 2023.
- [17] A. Papazafeiropoulos, P. Kourtessis, and S. Chatzinotas, “Max-Min SINR analysis of STAR-RIS assisted massive MIMO systems with hardware impairments,” *IEEE Trans. Wireless Commun.*, pp. 1–1, 2023.
- [18] J. An *et al.*, “Stacked intelligent metasurfaces for efficient holographic MIMO communications in 6G,” *IEEE J. Sel. Areas Commun.*, 2023.
- [19] X. Lin *et al.*, “All-optical machine learning using diffractive deep neural networks,” *Science*, vol. 361, no. 6406, pp. 1004–1008, 2018.
- [20] C. Liu *et al.*, “A programmable diffractive deep neural network based on a digital-coding metasurface array,” *Nature Electronics*, vol. 5, no. 2, pp. 113–122, 2022.
- [21] J. An *et al.*, “Stacked intelligent metasurfaces for multiuser downlink beamforming in the wave domain,” *arXiv preprint arXiv:2309.02687*, 2023.
- [22] Q.-U.-A. Nadeem, J. An, and A. Chaaban, “Hybrid digital-wave domain channel estimator for stacked intelligent metasurface enabled multi-user MISO systems,” *arXiv preprint arXiv:2309.16204*, 2023.
- [23] S. Abeywickrama *et al.*, “Intelligent reflecting surface: Practical phase shift model and beamforming optimization,” *IEEE Trans. Commun.*, vol. 68, no. 9, pp. 5849–5863, 2020.
- [24] Q. Nadeem *et al.*, “Intelligent reflecting surface-assisted multi-user MISO Communication: Channel estimation and beamforming design,” *IEEE Open J. Commun. Soc.*, vol. 1, pp. 661–680, 2020.
- [25] N. V. Deshpande *et al.*, “Spatially-correlated irs-aided multiuser FD mMIMO systems: Analysis and optimization,” *IEEE Trans. Commun.*, vol. 70, no. 6, pp. 3879–3896, 2022.
- [26] C. Wu *et al.*, “Channel estimation for STAR-RIS-aided wireless communication,” *IEEE Commun. Letters*, vol. 26, no. 3, pp. 652–656, 2021.
- [27] B. Zheng *et al.*, “A survey on channel estimation and practical passive beamforming design for intelligent reflecting surface aided wireless communications,” *IEEE Commun. Sur. & Tut.*, vol. 24, no. 2, pp. 1035–1071, 2022.
- [28] E. Björnson *et al.*, “Massive MIMO networks: Spectral, energy, and hardware efficiency,” *Foundations and Trends® in Signal Processing*, vol. 11, no. 3-4, pp. 154–655, 2017.
- [29] J. Hoydis, S. ten Brink, and M. Debbah, “Massive MIMO in the UL/DL of cellular networks: How many antennas do we need?” *IEEE J. Select. Areas Commun.*, vol. 31, no. 2, pp. 160–171, 2013.
- [30] A. K. Papazafeiropoulos and T. Ratnarajah, “Deterministic equivalent performance analysis of time-varying massive MIMO systems,” *IEEE Trans. Wireless Commun.*, vol. 14, no. 10, pp. 5795–5809, 2015.
- [31] A. K. Papazafeiropoulos, “Impact of general channel aging conditions on the downlink performance of massive MIMO,” *IEEE Trans. Veh. Tech.*, vol. 66, no. 2, pp. 1428–1442, Feb 2017.
- [32] S. Zhang and R. Zhang, “Capacity characterization for intelligent reflecting surface aided MIMO communication,” *IEEE J. Sel. Areas Commun.*, vol. 38, no. 8, pp. 1823–1838.
- [33] N. S. Perović *et al.*, “Achievable rate optimization for MIMO systems with reconfigurable intelligent surfaces,” *IEEE Trans. Wireless Commun.*, vol. 20, no. 6, pp. 3865–3882, 2021.
- [34] D. Bertsekas, *Nonlinear Programming*, 2nd ed., M. A. Scientific, Ed., 1999.
- [35] S. M. Kay, *Fundamentals of statistical signal processing: Estimation theory*. Upper Saddle River: Prentice Hall PTR, 1993.
- [36] A. Hjørungnes, *Complex-Valued Matrix Derivatives: With Applications in Signal Processing and Communications*. Cambridge University Press, 2011.